QUBIC: Measuring CMB polarization from Argentina

P. de Bernardis[1,2] P. Ade[3] G. Amico[1,2] D. Auguste[4] J. Aumont[5] S. Banfi[6,7] G. Barbarán[8] P. Battaglia[9,10] E. Battistelli[1,2] A. Baù[6,7] B. Bélier[11] D. Bennett[12] L. Bergé[13] J.-Ph. Bernard[14] M. Bersanelli[9,10] M.-A. Bigot-Sazy[15] N. Bleurvacq[15] J. Bonaparte[16] J. Bonis[4] G. Bordier[15] E. Bréelle[15] E. Bunn[16] D. Burke[12] D. Buzi[1,2] A. Buzzelli[17,18] F. Cavaliere[9,10] P. Chanial[15] C. Chapron[15] R. Charlassier[15] F. Columbro[1,2] G. Coppi[19] A. Coppolecchia[1,2] F. Couchot[4] R. D'Agostino[17,18] G. D'Alessandro[1,2] G. De Gasperis[17,18] M. De Leo[1,2] M. De Petris[1,2] A. Di Donato[16] L. Dumoulin[13] A. Etchegoyen[20] A. Fasciszewski[16] C. Franceschet[6,7] M.M. Gamboa Lerena[21] B. García[22] X. Garrido[4] M. Gaspard[4] A. Gault[23] D. Gayer[12] M. Gervasi[6,7] M. Giard[14] Y. Giraud-Heraud[15] M. Gómez Berisso[24] M. González[24] M. Gradziel[12] L. Grandsire[16] E. Guerrard[4] J.-Ch. Hamilton[15] D. Harari[24] V. Haynes[19] S. Henrot-Versillé[4] D.T. Hoang[15] F. Incardona[9,10] E. Jules[4] J. Kaplan[15] A. Korotkov[25] C. Kristukat[26] L. Lamagna[1,2] S. Loucatos[15] T. Louis[4] A. Lowitz[23] V. Lukovic[17,18] R. Luterstein[27] B. Maffei[28] S. Marnieros[13] S. Masi[1,2] A. Mattei[1,2] A. May[19] M. McCulloch[19] M. C. Medina[29] L. Mele[1,2] S. Melhuish[19] A. Mennella[9,10] L. Montier[14] L. M. Mundo[30] J. A. Murphy[31] J.D. Murphy[31] E. Olivieri[13] C. O'Sullivan[31] A. Paiella[1,2] F. Pajot[14] A. Passerini[6,7] H. Pastoriza[24] A. Pelosi[1,2] C. Perbost[15] O. Perdereau[4] F. Pezzotta[9,10] F. Piacentini[1,2] M. Piat[15] L. Piccirillo[19] G. Pisano[32] G. Polenta[1,2] D. Prêle[15] R. Puddu[1,2] D. Rambaud[14] P. Ringegni[30] G. E. Romero[29] M. Salatino[15] A. Schillaci[1,2] C. Scóccola[21] S. Scully[31] S. Spinelli[6,7] M. Stolpovskiy[15] F. Suarez[20] A. Tartari[15,33] J.-P. Thermeau[15] P. Timbie[23] S. Torchinsky[15] M. Tristram[4] V. Truongcanh[4] G. Tucker[34] C. Tucker[32] S. Vanneste[4] D. Viganò[9,10] N. Vittorio[17,18] F. Voisin[15] B. Watson[19] F. Wicek[4] M. Zannoni[6,7] A. Zullo[1,2]

[1] *List of institutions at the end*

Contact / paolo.debernardis@roma1.infn.it

Resumen / QUBIC (Interferómetro Bolométrico Q y U para Cosmología) es un ambicioso proyecto para medir la polarización del Fondo Cósmico de Microondas (CMB), que puede proporcionar información única sobre el universo primitivo y el proceso de inflación cósmica. El instrumento QUBIC combina la sensibilidad extrema de los bolómetros criogénicos y el control preciso de formación del haz y auto calibración de los interferómetros. El instrumento está siendo finalizado y calibrado para una primera instalación en el sitio de gran altura Alto Chorrillo (provincia de Salta, Argentina) a fines de 2018, y producirá, en los primeros dos años de operación, una medida sensible de la polarización del CMB, capaz de detectar una relación de tensor a escalar para modos-B $r < 0.01$.

Abstract / QUBIC (Q and U Bolometric Interferometer for Cosmology) is an ambitious project to measure the polarization of the Cosmic Microwave Background (CMB), which can provide unique information on the very early universe and the cosmic inflation process. The QUBIC instrument combines the extreme sensitivity of cryogenic bolometers and the accurate control of beam-forming and auto-calibration ability of interferometers. The instrument is being finalized and calibrated for a first installation at the Alto Chorrillo high altitude site (Salta province, Argentina) in late 2018, and will produce, in the first two years of operation, a sensitive measurement of CMB polarization, able to detect a tensor to scalar ratio for B-modes $r < 0.01$.

Keywords / cosmology — cosmic microwave background — polarization

1. Introduction

In the primeval plasma a huge number of photons was in equilibrium with matter ($\sim 10^9\gamma$/b). Equilibrium was maintained by Thomson scattering between photons and charged particles (mostly e^-). With the expansion of the universe, the photon/matter plasma cooled down, until H atoms could form (3 000 K, 380 000 yr after the big bang). The interaction of photons with neutral matter became negligible, and they were released, free to propagate without further interactions with matter. At that epoch, photons formed a 3 000 K blackbody, i.e. a bright background of optical and IR light filling the universe. Those photons are still filling the universe today, after an expansion of all distances (and wavelengths) by a factor 1100, and form a faint, cold background at mm wavelengths: it's the 2.735K blackbody of the CMB (Mather & et al., 1990). The CMB carries information about all the phases of the evolution of the Universe, from big-bang to structure formation and current clusters of galaxies, as demonstrated by a long series of CMB *anisotropy* experiments (see e.g. the results of the Planck mission, recently summarized in Planck Collaboration et al. 2016).

Precision measurements of the linear polarization state of the CMB (and in particular the so-called B-modes) provide information on the *cosmic inflation* process, basically happening at the big-bang, at energies of the order of 10^{19} GeV or more (see e.g. Kamionkowski & Kovetz 2016, and references therein). This is extremely interesting for both cosmology and fundamental physics, and a number of research groups worldwide are preparing sensitive experiments to extract this elusive information.

CMB photons are last scattered at recombination. It's a Thomson scattering, and any quadrupole anisotropy in the incoming photons induce linear polarization in the scattered photons. Density perturbations induce an irrotational linear polarization pattern (E-modes), which have been measured by several experiments. These density perturbations should be originated in the very early universe by the cosmic inflation process. The same process also produced tensor perturbations (gravitational waves). At recombination, tensor perturbations induce a small degree of polarization in the CMB, with both gradient and curl symmetries. The latter is called the B-mode. Moreover, lensing of E-modes by intervening matter concentrations between recombination and us also produces B-modes, important at small scales.

Polarization is a spin-2 quantity. The measured Q and U maps can thus be expanded in a spin-2 basis of modified spherical harmonics:

$$(Q+iU)(\vec{n}) = \sum_{\ell,m} (a^E_{\ell,m} \pm a^B_{\ell,m})_{\pm 2} Y_{\ell,m}(\vec{n}) \qquad (1)$$

from which the $a^E_{\ell,m}$ and $a^B_{\ell,m}$ can be retreived by inversion, so that the *angular power spectra* of CMB polarization c^{EE}_ℓ and c^{BB}_ℓ can be computed and thus separated and compared to theoretical expectations.

Since scalar perturbations do not produce B-modes, and lensing B-modes are produced mainly at small scales, B-modes at large scales are a signature of cosmic inflation. The amplitude of this signal is very small, but depends on the energy-scale of inflation. In fact the amplitude of tensor modes normalized to the scalar ones, r, is:

$$\left(\frac{r}{0.1}\right)^{\frac{1}{4}} \simeq \frac{V^{\frac{1}{4}}}{10^{16} GeV} \qquad (2)$$

where V is the inflaton potential, and

$$\sqrt{\frac{\ell(\ell+1)}{2\pi} c^{BB}_{\ell max}} \simeq 0.1 \mu K \left[\frac{V^{\frac{1}{4}}}{10^{16} GeV}\right]^2 \qquad (3)$$

There are theoretical arguments to expect that the energy scale of inflation is close to the scale of GUT, i.e. around 10^{16} GeV. So, if one actually detects primordial B-modes, then can constrain the energy-scale of inflation. Note, however, that the expected level of the signal is so low that noise, systematic effects and polarized foregrounds make this measurement incredibly challenging.

The current upper limits on B-modes at large scales are of the order of $r < 0.1$ (at 2σ). These have been obtained with a very significant effort of skilled experimentalists, building impressive *imaging polarimeters* for mm-waves based on bolometer arrays. QUBIC is also a polarimeter for mm-waves, but here interferometry is used to shape the bolometer array beams. Since systematic effects from the instrument ideally represent the final limit in this kind of measurements, it is very important to exploit orthogonal instrumental configurations to confirm any detection. For this very reason, and for its original setup, QUBIC is an important asset in the very competitive field of B-modes measurements.

2. Measuring the B-modes of the CMB

2.1. Survey sensitivity

mm-wave detectors for CMB measurements have been improved for decades. Cryogenic bolometers cooled at 0.3K or 0.1K have reached intrinsic NEP (Noise Equivalent Power) in the 10^{-17} - 10^{-18} $W/\sqrt{Hz}$ range, *i.e.* their noise is dominated by photon noise from the signal to be measured (and the contaminating background). In this limit, the only way to improve the sensitivity of the sky survey is to measure simultaneously many sky directions, using an array of detectors. In imaging telescopes, each element of the array looks at a different region of the sky, so that using N pixels the time required to survey a given sky area can be reduced by a factor N with respect to a single-detector observation. The sensitivity of the survey, for a given observation time, is thus improved by a factor $\sqrt{N}$. In the case of an interferometer, the use of N pixels has a very similar effect in the observation of the pattern of fringes produced by the entrance apertures array (see Hamilton et al. 2008). Modern CMB survey experiments (anisotropy and polarization) use large arrays of detectors (from hundred to a few thousands), whose size is limited by the difficulty of cooling a very large throughput system (including detectors, beam forming elements, and filters) at cryogenic temperatures. QUBIC makes no exception, using a 256 pixels detector array in the demonstrator configuration, and 4 of such arrays (1024 pixels) for each of the two focal planes of the first module of the final instrument (see below).

2.2. Polarization modulation

The first challenge of these measurements is how to modulate an extremely weak polarized signal in an overwhelming, structured unpolarized background. The first option is to use a mm-wave photometer array, add a polarizer in front of the detectors (or use an array of detectors selecting one polarization direction), and repeat the measurements for different rotations of the entire instrument around its optical axis. This was made with Planck and BICEP (just to mention two recent attempts), and several other experiments. The main disadvantage of this experimental configuration is that if the beam is slightly elliptical (as usually is), unpolarized sources offset from the beam center will be modulated as a linearly polarized source in the boresight. So an important *intensity to polarization leakage* is present and has to be corrected for. The second option is to start again with a mm-wave photometer array, and convert it into a Stokes polarimeter, i.e. add a Half-Wave-Plate (HWP) and a polarizer in the optical path, and rotate the HWP to modulate polarization (without modulating the intensity). This is the option used by several new experiments, including e.g. SPIDER, LSPE and QUBIC. If $S = (I, Q, U, V)$ is the Stokes parameters vector of the radiation being measured, $D = (1, 0, 0, 0)$ is the vector of the power-sensitive bolometric detector, P_V is the Mueller matrix of the vertical polarizer (in the restframe of the instrument), H is the Mueller matrix of the HWP, $R(\gamma)$ is the rotation matrix, and θ is the orientation of the polarized signal with respect to the horizontal axis in the restframe of the instrument, the radiation power on the detector for a given orientation γ of the HWP is

$$W = D \cdot P_V \cdot R(-\gamma) \cdot H \cdot R(\gamma) \cdot S \tag{4}$$

i.e.

$$W = \frac{1}{2}\left[I + Q\cos(4\gamma + 2\theta) + U\sin(4\gamma + 2\theta)\right]. \tag{5}$$

Here both the HWP and the polarizer have been assumed to be ideal. The linear polarized signal (Q, U) is thus modulated by the rotation of the HWP, while the unpolarized intensity I is not. The HWP can be rotated continuously ($\gamma = \dot{\gamma}t$), or in steps. The former is convenient to fight $1/f$-noise from fluctuating atmospheric emission and the detection chain, while the latter is simpler to implement in the instrument, since the HWP has to be cryogenically cooled to mitigate the effects of some of its non-idealities. In QUBIC we use a cryogenic, large-diameter, stepping HWP.

2.3. Beam forming

Arrays of CMB polarimeters work at mm-waves, where the beam shape is set by diffraction effects in the optics, in addition to detector properties. There are three classes of CMB polarimeters: imagers, coherent interferometers, bolometric interferometers. Coherent interferometers are too complex to implement for a large array of detectors: in fact we need arrays with thousands of pixels to achieve the required sensitivity. So we will consider only bolometric (Fizeau) interferometers in the following.

In a *Direct imager* the telescope is followed by an array of detectors in its focal plane. All recent CMB polarization instruments (but one) use this configuration. In a *Fizeau interferometer* there is an array of apertures (feedhorns at the wavelengths of interest here), whose signals are combined so that each aperture illuminates the entire detector array.

QUBIC uses this configuration, with significant advantages.

An array of detectors in the focal plane of an imager samples the image of the sky convolved with the beam response of the telescope. The beam size is defined by diffraction (the larger the telescope aperture the narrower the beam). The same array of detectors in the focal plane of a Fizeau interferometer samples the interference pattern produced by the sky. The image of the sky (if needed) can be retrieved by means of appropriate transforms (Fourier or similar). Note that the interference pattern reduces to the sky image in the limit of an infinite number of infinitesimal apertures. For a large but finite number of apertures, for each pixel the interferometer is equivalent to an imager with a *strange* multi-lobed beam, with a different shape for different pixels (synthesized beams). The size of the lobes is defined by the maximum distance between apertures (the larger the distance, the narrower the lobes). The number of lobes and their relative amplitude depends on the number of apertures. Despite of their complexity, these beams can be accurately calculated, and used for efficient map making (see e.g. Battistelli & QUBIC coll. 2011). There are other advantages of the interferometer configuration:

• There is a huge flexibility of the system, since one can decide to blank some of the apertures, thus changing the structure of all the beams in a well controlled way. This allows for self-calibration of instrument response, a standard technique in radio-interferometry, which can be used as well in bolometric interferometry. Beam patterns, beam efficiency, and even misalignments can be measured and corrected using the self-calibration procedure (see Bigot-Sazy et al. 2013).

• The fringes pattern depends on the phase shifts of radiation beams crossing different entrance apertures. For a given source shape, the phase shifts depend on the measured wavelengths. The synthesized beam of the interferometer is thus different for different wavelengths. This means that spectral information is present in the data and can be retrieved from the measured images of the fringes (QUBIC Collaboration, 2018). If the bolometers of the array are sensitive to a wide spectral band (e.g. the W band 80 to 110 GHz, or the D band 110 to 170 GHz, or the mm-window band 200 to 300 GHz), one can analyze the detected data dividing them in sub-bands (the more the sub-bands, the worse the sensitivity per-band).

2.4. Site selection

The Earth atmosphere is not perfectly transparent at CMB frequencies. Even in the *mm windows*, residual absorption and emission are present, due to the wings of H_2O, O_2, O_3 vibro-rotational lines. Moreover, atmospheric emission increases the photon background on the detectors and adds photon noise, while atmospheric turbulence adds significant 1/f noise. Two viable strategies have been used for sub-orbital CMB polarization experiments:

• Ground based operation, in sites with low and stable precipitable water vapor (PWV). These allow for long (years) integration time. The best sites are the South Pole and Dome-C in Antarctica, and a few high altitude locations in the Andes.

• Operation aboard of long-duration stratospheric balloon flights: these offer zero PWV, at the cost of limited (max. 1 month) integration time. Longer flights (up to 3 months with sealed balloons) are now becoming fea-

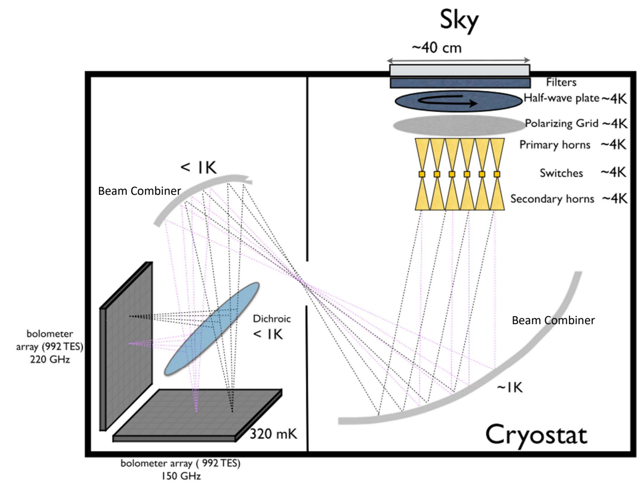

Figure 1: Block-diagram of the QUBIC instrument configuration.

sible, with some constraints on the total mass of the instrument. This option is certainly preferable at high frequencies (> 270 GHz), where atmospheric emission and absorption become very strong for ground-based observations.

QUBIC is a ground-based experiment, able to take data continuously for several years. It will be operated at the Alto Chorrillos mountain site (24°11′11.7″S; 66°28′40.8″W, altitude of 4869 m a.s.l.) selected for the LLAMA (Large Latin American Millimeter Array), near San Antonio de los Cobres, in the Salta province of Argentina. This site is not far (180 km) from the Chilean Atacama site, where other CMB experiments are very successfully operated. The cumulative distribution funcion for the zenith optical depth measured at the site at 210 GHz has $\tau_{210} < 0.1$ for 50% of the year, and $\tau_{210} < 0.2$ for 85% of the year, while usually mild winds (< 6 m/s for 50% of the year) suggest limited turbulence. The statistics for τ_{210} in Alto Chorrillos is worse than that of an Antarctic site (either South Pole or dome-C), but this disadvantage is compensated by easier site access and logistics. The tradeoff is also justified by the fact that a bolometric interferometer instrinsically rejects large-scale atmospheric gradients, which produce most of the atmospheric noise; moreover, atmospheric emission is not polarized to first order.

3. The QUBIC instrument

The instrument core configuration is sketched in Figure 1. The optics and the detection chain are entirely enclosed in a large cryostat, which is pointed at the sky region under observation by means of an alt-az mount. An additional degree of freedom allows for a rotation of the instrument around its boresight. This assembly is protected by a shelter, containing the power, operation, data acquistion, storage and communications electronics (see the sketch in Figure 2).

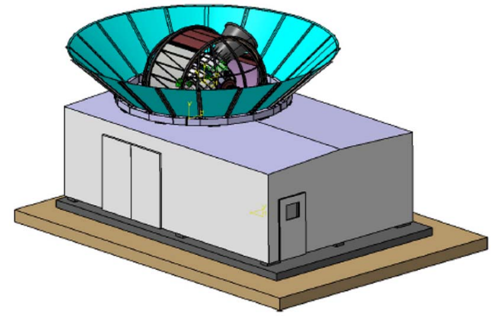

Figure 2: Rendering of the instrument and its protection shelter. The panels of the dome have been removed to show the instrument cryostat.

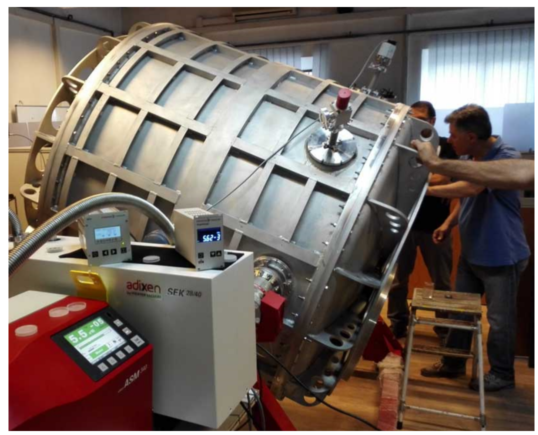

Figure 3: The vacuum shell of the QUBIC cryostat during testing.

3.1. The cryogenic system

The cryogenic system of QUBIC has a first stage based on a large aluminum vacuum shell and two 0.9W pulse tube (PT) refrigerators, cooling a large volume (~ 1 m^3) at 4K (see Figure 3).

The vacuum shell includes a large ($\sim$ 50 cm diameter, 20 mm thick) ultra-high molecular weight polyethylene window for the incoming radiation beam. The lightweight shell design is based on experience with ballon-borne cryostats (Masi et al., 1999). The 40K stage of the PT cools a radiation shield and a large thermal filter rejecting visible and near infrared radiation from the entrance beam. The 4K stage of the PT cools a second radiation shield, with a beam aperture including thermal and low-pass full-beam filters. The rotating waveplate and the grid polarizer are cooled by the same stage. The 40K and 4K shields are mechanically supported by trousses of fiberglass tubes. A large ^{4}He evaporation refrigerator (May et al., 2016) cools at $\sim$ 1K a further shield (the 1K box), thermally insulated from the 4K stage by means of stainless steel tubes. It also cools the large beam-combiner mirrors, and the dichroic filter splitting incoming radiation into two focal planes. A ^{3}He evaporation refrigerator (May et al., 2016) cools at 0.3K the detector arrays, including their

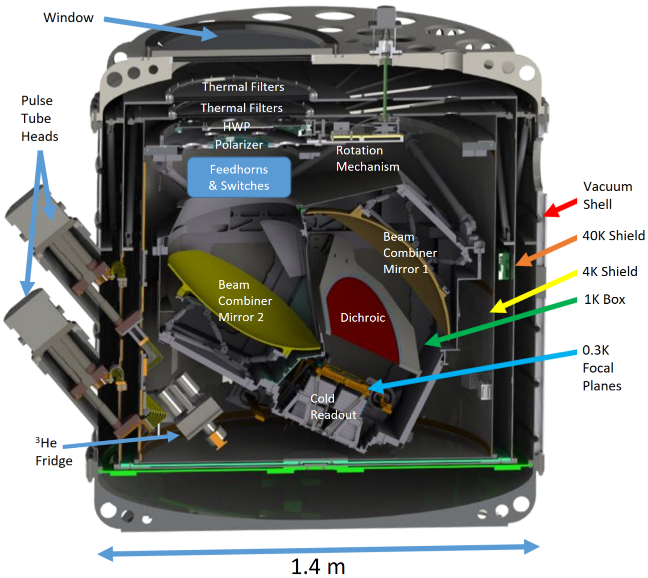

Figure 4: Rendered cut view of the QUBIC receiver. All the main subsystems cooled by the cryogenic system are labeled in the figure.

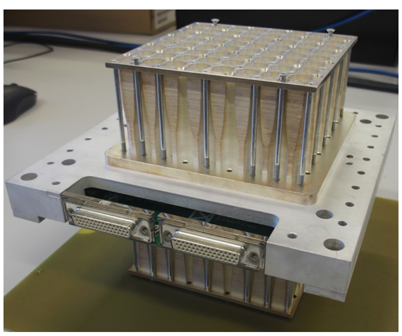

Figure 5: 8×8 150GHz array of horns, bracketing the array of switches, for the QUBIC demonstrator. The horns are produced stacking precision-cut metal platelets.

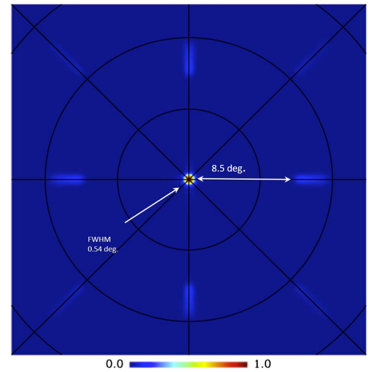

Figure 6: Simulation of the synthesized beam of the center pixel of the 150 GHz array, taking into account the finite (30%) bandwidth of the detectors. The beams of peripheral pixels are more complex and less symmetric, with side beams efficiency higher than the boresight beam.

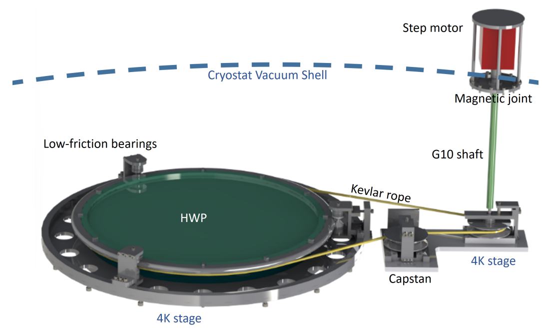

Figure 7: Sketch of the cryogenic rotator for the QUBIC HWP. Not shown: optical fibers and optical encoder for position readout.

optical filters and proximity electronics. In Figure 4 we show the internal configuration of all the main subsystems cooled by the QUBIC cryostat. The total mass to be cooled at 1K is of the order of 150 kg. We use efficient heat switches to reduce the cooling time to less than 10 days.

3.2. The optical system

400 co-aligned primary horns form the array of apertures of the interferometer (Figure 5). The horns are fabricated using the platelets technique (see e.g. Del Torto et al. 2011). Each aperture is composed of a front horn collecting radiation from the sky, a RF switch, and a back horn illuminating the entire focal plane array of bolometric detectors through a beam-combining optical system.

In the first module of QUBIC two focal-plane arrays of detectors are illuminated by the beam-combiner: one receives radiation reflected from the dichroic, the other receives transmitted radiation. The transmitted array is sensitive to the 150 GHz band, the reflected one is sensitive to the 220 GHz band. The pattern of fringes formed on the focal planes depends on the brightness distribution of the observed sky. In time-reverse, each bolometer in the focal plane array illuminates cophasally the entrance apertures array. The sensitivity to radiation coming from different directions of the sky (synthesized beam) can be computed taking into account the primary beam defined by the horns, the interference due to the different phase delays of source radiation arriving at different horns, and the additional sidelobes rejection provided by the forebaffle and the ground shield. An example is shown in Figure 6.

Polarization sensitivity is obtained by means of a rotating HWP, followed by a wire-grid polarizer. The HWP is stepped by a cryogenic mechanism, which is an improved version of the one described in Salatino et al. (2011). The general design of the rotator is shown in Figure 7.

3.3. The detection chain

Each focal plane is composed by four 256-pixels arrays (Figure 8) of Nb_xSi_{1-x} transition edge sensors

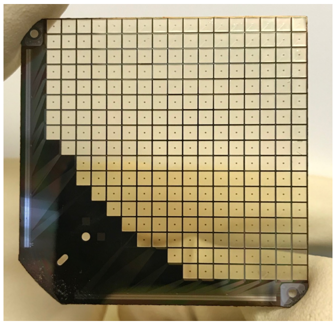

Figure 8: Picture of one 256-pixels Nb_xSi_{1-x} TES bolometer array for QUBIC. The pixel pitch is 3 mm.

(TES) with a critical temperature around 500 mK. These bolometers are optimized for a 5-50 pW background (for the 150-220 GHz windows) suspending the Pd-grid absorbers and the thermistors on a 500 nm thin SiN membrane, resulting in a thermal conductivity between 50 and 500 pW/K. The total noise equivalent power (NEP) of these detectors is $\sim 5{\times}10^{-17} W/\sqrt{Hz}$, with a time constant between 10 and 100 ms. The two thermistors ends are routed to the edge of the wafer by means of superconducting Al lines, and connected via wire-bonds to the front-end electronics. The TESs are voltage-biased to exploit strong electrothermal feedback. The current readout is based on SQ600S squids which also allow for 128:1 time-domain multiplexing, using cryogenic ASIC low noise amplifiers (Aumont et al., 2016).

A picture of the cryogenic section of the detection chain assembled is shown in Figure 9.

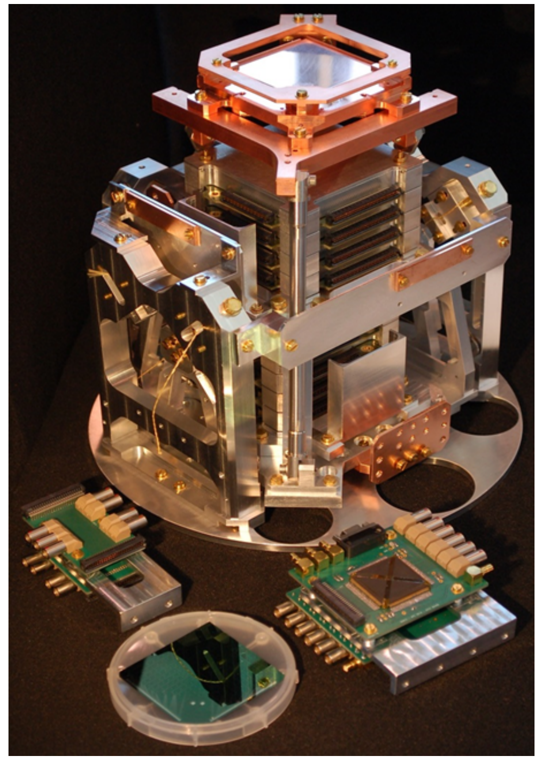

Figure 9: The cryogenic section of the QUBIC detection chain.

4. Calibrations and observations

A detailed plan is in place to fully characterize the performance of the QUBIC instrument before and after delivery to the site. These include detectors absolute response, intercalibration and cross talk, band-pass and leakage spectral measurements, synthetic beam reconstruction, polarisation angle recovery, self-calibration checks, time constants, detector linearity, NEP (slope and f-knee values of the noise spectrum), EMI/EMC.

During observations, QUBIC will alternate two operation modes: self-calibration and sky measurement.

In the *self calibration mode*, the instrument points to artificial polarized sources (coherent microwave oscillators for both bands with 1 to 5 mW power, located on top of a calibration tower $\sim$ 45m high and $\sim$ 45m away from the instrument). Meanwhile, the switches of the feedhorns are operated to close the entrance apertures two by two, allowing to analyze the performance of the system and identify systematic effects, as described in Bigot-Sazy et al. (2013). The sources are optimized to produce very high S/N ($\sim$ 20 000) signals, while not saturating the detectors. The time allocated for self-calibration will be significant (up to 50% of the total useful time, depending on the performance of the instrument).

In the *sky measurement mode* QUBIC will scan at constant elevation over low-dust regions in the southern hemisphere, including the BICEP2 region (RA=0^o, dec=-57^o) and the Planck clean field (RA=8.7^o, dec=-41.7^o). When observed from Alto Chorrillos, the centers of these two regions change their elevation in the range 30^o-60^o and 30^o-70^o respectively, matching the allowed elevation range for the operation of the PTs.

The instrument will typically scan in azimuth around the center of the selected field with a typical azimuth range of $\pm 15^o$, and a speed $\sim 1^o/s$. The elevation is updated after typically 10 scans to track the elevation of the center of the field. At the end of each scan the HWP is stepped by 15^o. Additionaly, QUBIC is rotated in steps around its optical axis (details to be defined) to check for systematic effects. This scanning strategy allows to cover $\sim$ 1% of the whole sky in 24 hours. With this sky coverage, measurements of the B-modes at multipoles $\ell < 100$ are obtained.

5. Performance forecast

End-to-end simulations of the performance of the first module of QUBIC have been carried out (see Aumont et al. 2016 for details), assuming reasonable treatment of foregrounds (which are removed using the two bands of QUBIC and, optionally, also the data of the polarization survey of Planck at 353 GHz) and a conservative 30% time efficiency due to weather in Alto-Chorrillos, and 6 to 12 hours per day for self-calibration. The expected sensitivity to the tensor-to-scalar ratio r after 2 years of observations is $\sigma_r \sim 0.01$ (see Figure 10).

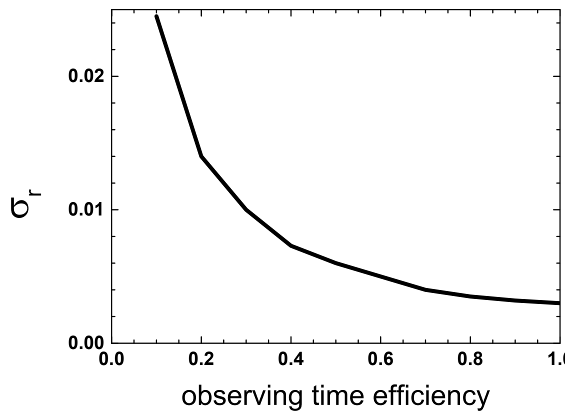

Figure 10: Expected error on the estimate of the tensor to scalar parameter r for 2 years of operation of QUBIC, versus observing time efficiency. If for 30% of the time the weather is excellent (a reasonable assumption for the selected observing site), $\sigma_r \sim 0.01$. This estimate is based on end-to-end simulations, including foreground removal by template fitting on the two bands of QUBIC (150 and 220 GHz).

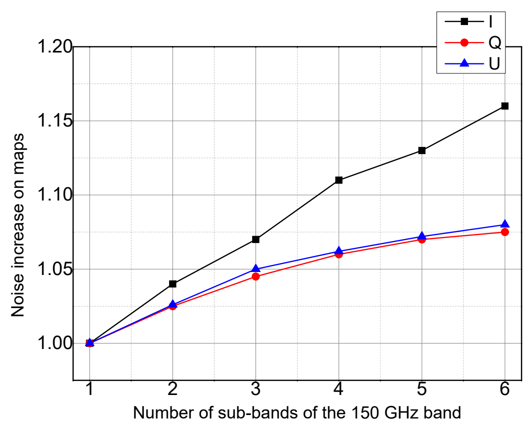

Figure 11: Noise increase in the I, Q, U maps as a function of the number of sub-bands obtained fractioning the original 150 GHz band.

Additional simulations have been performed to analyze the performance of QUBIC as a spectropolarimeter, exploiting the frequency-dependance of the synthetic beam across the bands. In figure 11 it is shown that the penalty for dividing a measurement band in sub-bands is modest, so that spectropolarimetry is really within reach of QUBIC, improving significantly the ability to separate genuine CMB polarization from contaminating foregrounds.

In figure 12 we report the results of end-to-end simulations of the QUBIC results from 2 years of operation of the full instrument. Using the Spectro-Imaging capabilities of QUBIC we can reconstruct three sub-bands within our physical 150 GHz filter and 2 sub-bands in the 220 GHz one. From these 5 maps, we can build 5 B-modes angular power spectra that are

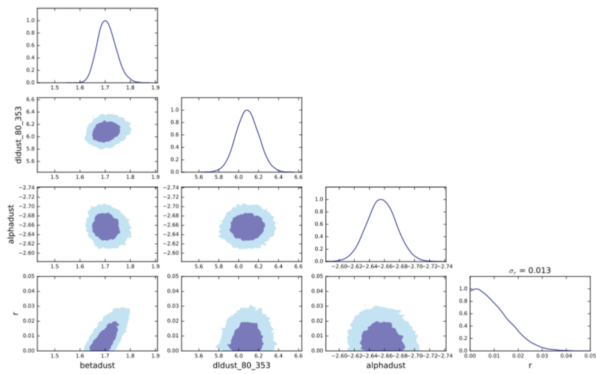

Figure 12: Likelihoods and joint-likelihoods for the determination of the tensor to scalar ratio r, the amplitude of dust fluctuations, and the spectral index of the dust after two years of operation of the QUBIC full instrument (see text).

input in a maximum-likelihood minimization over the tensor-to-scalar ratio r (on the bottom right) as well as on a three-parameters B-modes dust emission model (from latest Planck studies) on the left part. The input primordial B-modes were set to r=0 and we see that we indeed find a maximum-likelihood at r=0 showing that the dust removal was efficient using the 5 QUBIC bands. The width of the likelihood on r shows a sensitivity $\sigma(r) = 0.013$. This shows both the sensitivity and the ability to control foreground emission using spectro-imaging.

6. Conclusions

The B-mode search is a highly competitive effort involving many teams worldwide and significant resources with "stage-3" experiments like, e.g., BICEP3, Keck Array, CLASS, POLARBEAR, SPTPol, ACTPol, EBEX, SPIDER, LSPE, and with the forthcoming "stage-4" experiments. All these instruments are imagers. QUBIC follows a different approach - bolometric interferometry - with totally different (and well controllable) systematic effects. In this respect, QUBIC assumes extreme importance, since only independent detections of B-modes obtained with orthogonal experiments will provide the required evidence for this elusive observable.

QUBIC is in an advanced, intense development phase, aiming at a full performance demonstration in the first half of 2018, and delivery to the Alto Chorrillos site in the second half of the same year. After commissioning and two years of nominal operation at the site, the experiment promises to deliver high quality CMB polarization data at 150 and 220 GHz, improving the sensitivity to B-modes by almost one order of magnitude with respect to current experiments, with very effective systematics control features.

The scalability of the QUBIC concept is such that QUBIC could evolve towards a European stage-4 CMB polarization experiment, with mutiple modules allowing for a $\sigma(r) \sim 0.001$ by 2025.

References

Aumont J., et al., 2016, ArXiv e-prints 1609.04372
Battistelli E., QUBIC coll. 2011, Astrop. Phys., 34, 705
Bigot-Sazy M.-A., et al., 2013, A&A, 550, A59
Del Torto F., et al., 2011, JINST, 6, 6009
Hamilton J.-C., et al., 2008, A&A, 491, 923
Kamionkowski M., Kovetz E. D., 2016, ARA&A, 54, 227
Masi S., et al., 1999, Cryogenics, 39, 217
Mather J. C., et al. 1990, ApJL, 354, L37
May A. J., et al., 2016, in Adv. in Optical and Mech. Tech. for Telescopes and Instr. II, SPIE proc.. p. 991266
Planck Collaboration et al., 2016, A&A, 594, A1
QUBIC Collaboration 2018, in preparation
Salatino M., de Bernardis P., Masi S., 2011, A&A, 528, A138

List of institutions

[1] Dipartimento di Fisica Sapienza Universitá di Roma
[2] INFN Sezione di Roma
[3] Cardiff University
[4] Laboratoire de l'Accélérateur Linéaire, Orsay (CNRS-IN2P3)
[5] Institut d'Astrophysique Spatiale, Orsay (CNRS-INSU)
[6] Dipartimento di Fisica, Universitá di Milano – Bicocca
[7] INFN Sezione di Milano-Bicocca
[8] Regional Noroeste (CNEA)
[9] Dipartimento di Fisica, Universitá degli studi di Milano
[10] INFN Sezione di Milano
[11] Centre de Nanosciences et de Nanotechnologies, Orsay
[12] National University of Ireland, Maynooth
[13] Centre de Spectrométrie Nucléaire et de Spectrométrie de Masse, Orsay (CNRS-IN2P3)
[14] Institut de Recherche en Astrophysique et Planétologie, Toulouse (CNRS-INSU)
[15] Astroparticule et Cosmologie, Paris (CNRS-IN2P3)
[16] Centro Atómico Constituyentes (CNEA)
[17] Universitá di Roma Tor Vergata
[18] INFN Sezione di Roma Tor Vergata
[19] University of Manchester
[20] Instituto de Tecnologías en Detección y Astropartículas (CNEA, CONICET, UNSAM)
[21] Facultad de Cs Astronómicas y Geofísicas (Universidad Nacional de La Plata)
[22] Instituto de Tecnologías en Detección y Astropartículas (CNEA, CONICET, UNSAM)
[23] University of Wisconsin, Madison
[24] Centro Atómico Bariloche and Instituto Balseiro (CNEA)
[25] Brown University, Providence
[26] Escuela de Ciencia y Tecnología (UNSAM)
[27] Regional Noroeste (CNEA)
[28] Institut d'Astrophysique Spatiale, Orsay (CNRS-INSU)
[29] Instituto Argentino de Radioastronomía (CONICET, CIC)
[30] GEMA (Universidad Nacional de La Plata)
[31] National University of Ireland, Maynooth
[32] Cardiff University
[33] INFN Sezione di Pisa
[34] Brown University, Providence